*J. Fluid Mech.* (1993), *vol.* 249, *pp.* 135–159



# Rotating Rayleigh–Bénard convection: asymmetric modes and vortex states

By FANG ZHONG†, ROBERT E. ECKE AND VICTOR STEINBERG‡

Physics Division and Center for Nonlinear Studies, Los Alamos National Laboratory, Los Alamos, NM 87545, USA

(Received 19 April 1992 and in revised form 12 October 1992)

We present optical shadowgraph flow visualization and heat transport measurements of Rayleigh–Bénard convection with rotation about a vertical axis. The fluid, water with Prandtl number 6.4, is confined in a cylindrical convection cell with radius-to-height ratio $\Gamma = 1$. For dimensionless rotation rates $150 < \Omega < 8800$, the onset of convection occurs at critical Rayleigh numbers $R_c(\Omega)$ much less than those predicted by linear stability analysis for a laterally infinite system and qualitatively consistent with finite-aspect-ratio, linear-stability calculations of Buell & Catton (1983). As in the calculations, the forward bifurcation at onset is to states of localized flow near the lateral walls with azimuthal periodicity of $3 < m < 8$. These states precess in the rotating frame, contrary to the assumptions of Buell & Catton (1983) but in quantitative agreement with recent calculations of Goldstein *et al.* (1992), with a frequency that is finite at onset but goes to zero as $\Omega$ goes to zero. At $\Omega = 2145$ we find primary and secondary stability boundaries for states with $m = 4$, 5, 6, and 7. Further, we show that at higher Rayleigh number, there is a transition to a vortex state where the vortices form with the symmetry of the existing azimuthal periodicity of the sidewall state. Aperiodic, time-dependent heat transport begins for Rayleigh numbers at or slightly above the first appearance of vortices. Visualization of the formation and interactions of thermal vortices is presented, and the behaviour of the Nusselt number at high Rayleigh numbers is discussed.

## 1. Introduction

Thermal convection in a layer of fluid heated from below and rotated about a vertical axis is a simple model that contains the fundamental forces that control atmospheric and oceanic circulation. In addition, the multiple control parameters of heating and rotating form an interesting system for the study of hydrodynamic stability, bifurcations, and turbulence. The control parameters for this problem are the Rayleigh number $R \equiv g\alpha d^3 \Delta T/\nu\kappa$, where $g$ is the acceleration due gravity, $\alpha$ is the thermal expansion coefficient, $\Delta T$ is the temperature difference across the fluid layer of height $d$, $\nu$ is the kinematic viscosity, and $\kappa$ is the thermal diffusivity, and the dimensionless rotation rate $\Omega = \Omega_D d^2/\nu$, where $\Omega_D$ is the physical angular rotation frequency. Some properties of convection are also influenced by the Prandtl number, $\sigma \equiv \nu/\kappa$. An additional constraint that plays an important role in experiments on rotating convection is the aspect (radius-to-height) ratio $\Gamma \equiv r_0/d$ where $r_0$ is the

† Present address: Department of Physics, Duke University, Durham, NC 27706, USA.

‡ Permanent address: Department of Nuclear Physics, Weizmann Institute of Science, Rehvot, Israel.

radius of a cylindrical convection cell. The rotation adds centrifugal and Coriolis terms to the equations of fluid motion. In most theoretical treatments, however, the centrifugal force is neglected by assuming that it is small compared to gravity, i.e. $\Omega_D^2 r_0/g \ll 1$.

Linear stability of rotating convection for a laterally infinite system was first considered by Chandrasekhar (1953, 1961) and by Veronis (1959). For $\sigma > 0.68$ the onset should be stationary and the overall effect of rotation is to stabilize the conduction state and to increase the critical Rayleigh number $R_c$ for the onset of convection. This can be understood intuitively as a consequence of the Taylor–Proudman theorem which indicates that three-dimensional motions, such as formed by convection rolls or cells, are suppressed in rotating systems. Other theoretical papers describe various aspects of rotating convection, some of which seek to explain specific features of physical experiments on this system. We discuss the experiments and theoretical interpretations appropriate to the fluid used in our experiments which had $\sigma = 6.4$.

An interesting complication to the linear theory is that for $\Omega > \Omega_c$ Küppers & Lortz (1969) showed that any two-dimensional parallel-roll convection state is unstable with respect to rolls oriented at an angle of about 60° relative to the initial rolls. Küppers (1970) later calculated the dependence of $\Omega_c$ on $\sigma$, showing that it decreased with decreasing $\sigma$ so that $\Omega_c = 22.5$ for water with $\sigma = 7$. The Küppers–Lortz (KL) transition leads to noisy time-dependent convection at onset for $\Omega > \Omega_c$. On the basis of this instability one would expect such time dependence for our experiments in which $\Omega \gg \Omega_c$.

Previous experimental work on rotating thermal convection was based primarily on heat transport data or on qualitative flow visualization. Early work using water (Nakagawa & Frenzen 1955) supported general trends of the linear theory. The detailed heat transport measurements of Rossby (1969) provided the first quantitative comparisons with theoretical predictions. For water the results for the convective onset were consistent with the linear theory for $\Omega \leqslant 130$ but did not agree for larger values of $\Omega$. In particular the Nusselt number data, $Nu \equiv K/K_c$ where $K$ is the effective conductivity of the fluid and $K_c$ is the thermally diffusive conductivity, showed that the onset of convection was progressively lowered relative to the linear theory as $\Omega$ increased; at $\Omega = 5000$ the convective onset occurred a factor of three below the predicted value. Another result was that for large $\Omega$ the $Nu$ data close to onset were sensitive to the aspect ratio (see figure 12 in Rossby 1969) although the onset value was not. Similar low onset values were obtained by Pfotenhauer, Niemela & Donnelly (1987) for rotating convection in helium which has $\sigma \approx 0.6$. A number of possible explanations have been explored theoretically and numerically, including finite-amplitude instability and centrifugal effects, but most cannot account for the experimental observations (see Pfotenhauer *et al.* 1987 for a good review). An important consideration to note here is that to avoid centrifugal effects, which are proportional to $\Omega_D^2$, the absolute rotation speed needs to be low. Therefore, to achieve the high *dimensionless* rotation rates of interest here, one must decrease the viscosity $\nu$ or increase the depth of the fluid. In practice large $\Omega$-values are obtained by increasing the depth of the layer, resulting in a reduction of the cell aspect ratio. Thus it is important to appreciate the role of finite size in understanding the phenomena that occur in real convection cells.

The influence of geometry and, in particular, the aspect ratio was not considered in detail in early theoretical investigations of rotating convection because the canonical wisdom derived from non-rotating convection was that sidewalls stabilize

the conduction state and increase the critical Rayleigh number $R_c$ (Charlson & Sani 1970; Stork & Müller 1975). Calculations by Buell & Catton (1983) showed, however, that for rotating, small-aspect-ratio, cylindrical convection cells, the conduction solution was linearly unstable with respect to azimuthally-periodic modes spatially localized near the outer boundary. On the basis of a careful analysis of possible effects of overstability, finite-amplitude instability, and centrifugal forces, Pfotenhauer *et al.* (1987) concluded that these asymmetric mode states were the probable cause of the much lower $R_c$-values observed in experiments. Without visualization, however, this conjecture could not be tested directly. Similarly, Rossby used a visualization scheme (aluminium flakes) that did not allow imaging of the flow in the region of interest.

In addition to theoretical and experimental investigations of convection for the linear and weakly nonlinear states near onset, there has been recent interest in turbulent convection with rotation. Boubnov & Golitsyn (1986, 1991) made measurements and some visualizations of rotating convection with an open top surface and qualitatively characterized vortex states and vortex interactions. Experimental measurements by Fernando, Chen & Boyer (1991) concentrated on describing the vertical velocity profile and other statistical properties of the turbulent state. There have also been some numerical calculations of turbulent rotating convection (Raasch & Etling 1992) that show striking vortex dynamics and coherent structures. Further, it is interesting to consider the influence of rotation on the scaling of turbulent heat transport and on the probability distribution functions for temperature and velocity. Recent experimental (Heslot, Castaing & Libchaber 1987; Wu & Libchaber 1992; Solomon & Gollub 1991) and theoretical (Castaing *et al.* 1989; Shraiman & Siggia 1990) work has focused considerable effort on understanding the advection of temperature by the turbulent velocity field and on the 'non-classical' scaling of Nusselt number with Rayleigh number. Classical theories (Malkus 1954*a*, *b*; Howard 1966) of convective heat transport predicted that $Nu \propto R^{\frac{1}{3}}$ whereas precise measurements in helium gas over many orders of magnitude in $R$ (Threlfall 1975; Heslot *et al.* 1987) clearly show scaling with an exponent of $\frac{2}{7}$. A recent theory (L'vov 1991) showed that conservation of entropy flux determines the scaling of the energy–wavevector distribution in convection, producing a different scaling than the $k^{-\frac{5}{3}}$ power law of isotropic, homogeneous turbulence. Such arguments suggest that the additional terms in the inertial equations arising from rotation can further modify the relevant scaling behaviour. For this and other reasons relating to the coherence of thermal plumes, rotating convection provides a useful model system for fundamental studies of turbulence.

In this work, we present heat transport data, flow visualization, and local temperature measurements that characterize the convective state in a $\Gamma = 1$ cylindrical container, bounded above and below by isothermal surfaces, from very close to onset up to the turbulent regime. Our results explain a number of long-standing problems in rotating convection and confirm, using flow visualization, the presence of azimuthally periodic modes at onset for high $\Omega$. We also demonstrate for the first time the existence of vortex structures in containers with rigid top and bottom boundaries. Our results are organized as follows. In §2 we describe the experimental apparatus. In §3 we present data for the convective onset and visualization of the azimuthally periodic states. These azimuthal modes were observed to precess in the rotating frame (Zhong, Ecke & Steinberg 1991; Ecke, Zhong, Knobloch 1992) and a detailed description of the precession frequency and mode-number dependence of the travelling wave state is presented. For values of $R$

several times larger than $R_c$ vortex structures appear in the central region of the cell as discussed in §4. We also present properties of vortex creation and merger in the turbulent regime and describe analysis of the heat transport data for a range of $\Omega$- and $R$-values. Conclusions in §5 include unanswered questions, opportunities for theoretical investigation, and some discussion about the aspect-ratio dependence of the phenomena we observe.

## 2. Experimental apparatus

Our experiments on rotating thermal convection were performed in an apparatus that consisted of a rotating thermal convection cell and stationary surrounding cooling bath and shadowgraph optics. This arrangement has certain limitations compared with a rotating table approach but proved adequate for many of our measurements. We discuss these aspects below, starting with the convection cell, proceeding to thermal measurements and ending with a description of the optical shadowgraph apparatus.

The convection cell was cylindrical with radius $r_0 = 5.005$ cm and height $d = 4.993$ cm. It was constructed with 0.39 cm thick Plexiglas sidewalls, a 12.7 cm diameter, 0.32 cm thick sapphire top plate, and a 0.64 cm thick hard-nickel-plated copper bottom boundary, figure 1. The top plate was maintained at fixed temperature $T_{top} = 23.8$ °C with stability $\pm 0.25$ mK r.m.s. by water flow that was evenly distributed by a set of jets and channels (Meyer 1988). A set of thermistors placed around the edge of the top plate measured an average top-plate temperature, $T'_{top}$. The bottom plate was heated with a fixed heat current provided by a 90 Ω, spatially distributed film heater. Its temperature $T'_{bot}$ was measured by a thermistor embedded in the centre and at the vertical midplane of the plate. Closed-cell foam insulation surrounded the sidewalls and the bottom plate to prevent radiation and conduction/convection heat loss to the outer can. The outer can was stainless steel and was maintained in the feedback temperature bath to about the same limits as the top plate. The electrical leads were thermally anchored on the bottom of the can and then passed through a rotating slip-ring connector located on the drive shaft that provided rotation to the can/cell unit. Power applied to the film heater was measured by sensing the voltage across the heater and by separately determining the heater current by measuring the voltage across a calibrated, temperature-controlled reference resistor.

Heat transport in thermal convection is typically reported in terms of the Nusselt number $Nu$. In the conduction state $Nu = 1$ and in the convecting state $Nu > 1$. In experiments heat is also conducted across the temperature difference $\Delta T$ through the sidewalls and along other parasitic heat paths which we call background. Assuming that the conductance of the water is given (International Critical Tables 1930), the contribution from this background conductivity is accounted for in the calculation for $Nu$ so that only the fluid portions remain. The precision of the Nusselt number measurements is a function of $\Omega$ since $\Delta T_c$ ($\Delta T$ at the onset of convection) varies from about 0.07 K at $\Omega = 2145$ to less than 1 mK for the non-rotating case. Our stability in top-plate temperature of about 0.2 mK yields 0.3% precision for $\Omega = 2145$ but 50% at $\Omega = 0$. Thus we could not reliably determine $\Delta T_c$ for $\Omega < 100$. Although the absolute stability of the heat transport measurements was limited by long-term stability of the top-plate temperature, the short-term temperature fluctuations in the bottom plate were only 0.02 mK r.m.s. This allowed us to determine very small-amplitude time dependence that develops as $\Delta T$ is increased.

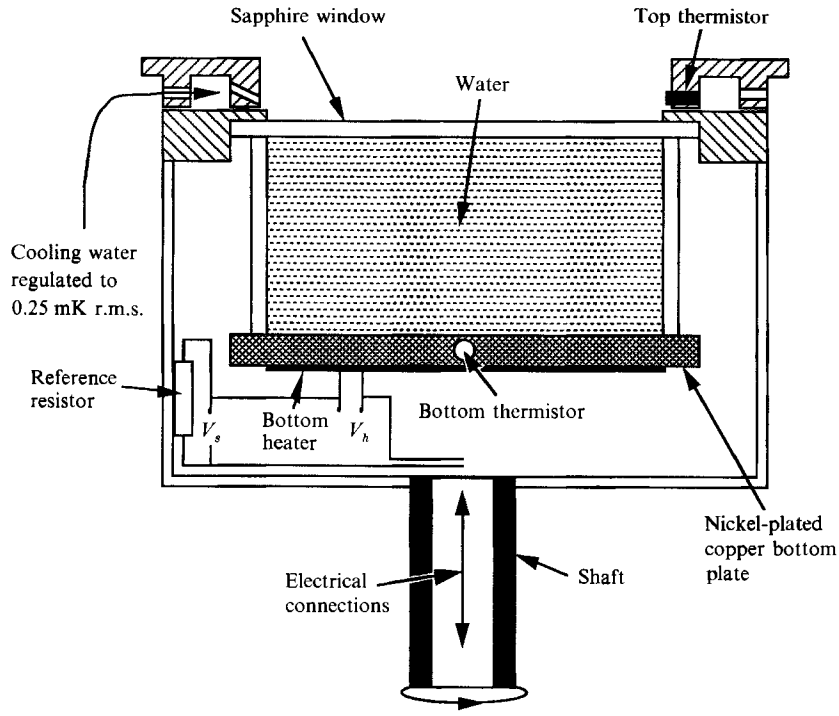


FIGURE 1. Illustration of the Rayleigh–Bénard convection cell.

Rotation was provided by a stepping motor that drove a flexible belt attached to the shaft. A gear assembly allowed the motor to operate at reasonably high frequency so as to avoid the jitter associated with digital stepping motors. In addition, microstepping reduced this effect so that it was not a factor in the rotation. Rotation frequencies were in the range 0.01 to 0.5 Hz with the speed determined to be steady to $\pm 0.0001$ Hz. Early in the experiment the stepping motor was driven by a separate controller board, whereas later a module was driven directly from a frequency generator in the computer thereby allowing for programmed control of the rotation speed.

Flow visualization was achieved using optical shadowgraph visualization of the temperature field. Recent enhancements of this standard technique including digital image processing have made it a powerful tool for studying the convective instability. Until this work, however, optical shadowgraph visualization has been used almost exclusively (for an exception see Busse 1981) for convection in thin fluid layers, 1–5 mm. We have used the technique to study patterns and vortex structures in deep cells of water where $d = 5$ cm. The sensitivity of the shadowgraph method is lower for deep layers and therefore the distance from onset that a pattern can be detected is substantially greater than for thin layers. Whereas it has become straightforward to detect patterns in thin layers to within better than 0.2% of onset, our visualization is limited to about 30% above onset. This is adequate for our purposes and is much better than visualization with dye or aluminium flakes. We use the afocal shadowgraph arrangement (Croquette 1986; Kolodner & Williams 1990) and a CCD video camera, figure 2, to obtain images of the flow. As a consequence of the rotation of the convection cell and the stationary structure of the shadowgraph optics and video camera, we captured a single frame each full revolution of the cell.

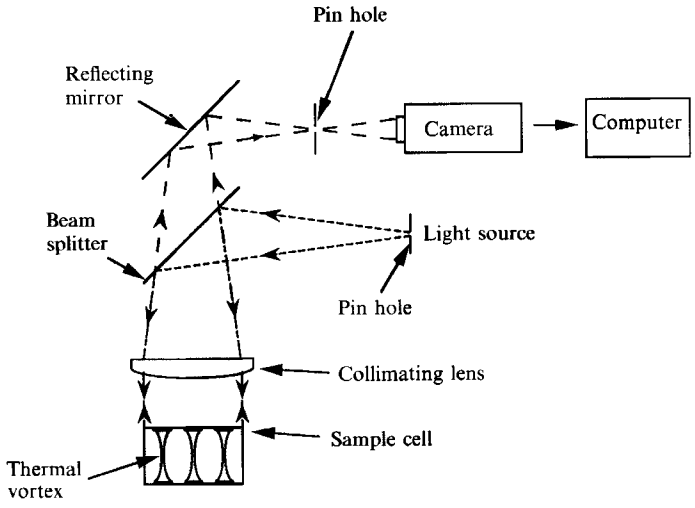


FIGURE 2. Illustration of shadowgraph visualization optics.

This was accomplished by strobing the digitizer with a signal from a shaft encoder. The evolution times for the convective states were sufficiently long that this was not a problem except for the most dynamic states in the turbulent regime.

Several comments should be made about the evaluation of fluid parameters used in the analysis of the results presented. Because a constant heat current was applied to the bottom plate, its temperature was time dependent for time-dependent heat transport. Rayleigh numbers were therefore evaluated as a time average over $\Delta T(t)$. Second, the top-plate temperature was fixed and thus $T_{\rm bot}$ increased monotonically with increased heat current. This resulted in an increasing mean cell temperature. Most fluid parameters were evaluated at the mean cell temperature for a particular heat current, the exceptions being $\Omega$ and $\sigma$. $\Omega$ was calculated from the fixed angular frequency $\Omega_{\rm D}$ using $\nu(T)$ evaluated at the mean temperature at onset. Because $\nu$ for water is a rather strongly decreasing function of $T$ the values for $\Omega$ will be slightly higher above onset. The deviation arising from this is less than 1% for all data for which $\epsilon < 10$. At the highest values of $R \approx 10^7$ this correction can be as large as 10%. The Prandtl number was $\sigma = 6.4$ evaluated for $T_{\rm bot} = 23.8$ °C.

One final feature was added to the convection cell to help resolve questions about the time dependence of the onset states. Two high-sensitivity thermistors were embedded in the sidewall at the midplane. These local sensors were used to measure time-dependent convection and to detect any convective structures travelling in the azimuthal direction. We describe them in more detail below after we have discussed the onset modes.

## 3. Convective onset and azimuthal modes

The onset of convection in the $\Gamma = 1$ cylindrical cell used in this study was determined by measurement of the heat transport. In figure 3, the Nusselt number is shown for $\Omega = 2145$ as a function of a reduced bifurcation parameter $\epsilon \equiv (R - R_{\rm c}(\Omega))/R_{\rm c}(\Omega)$. The onset is a forward bifurcation at $R_{\rm c}$ ($\epsilon = 0$) and there are several different branches above onset which are reproducible and correspond to states with different azimuthal wavenumber as discussed below. The values of $R_{\rm c}$ determined from a series of such measurements at numerous $\Omega$-values define the

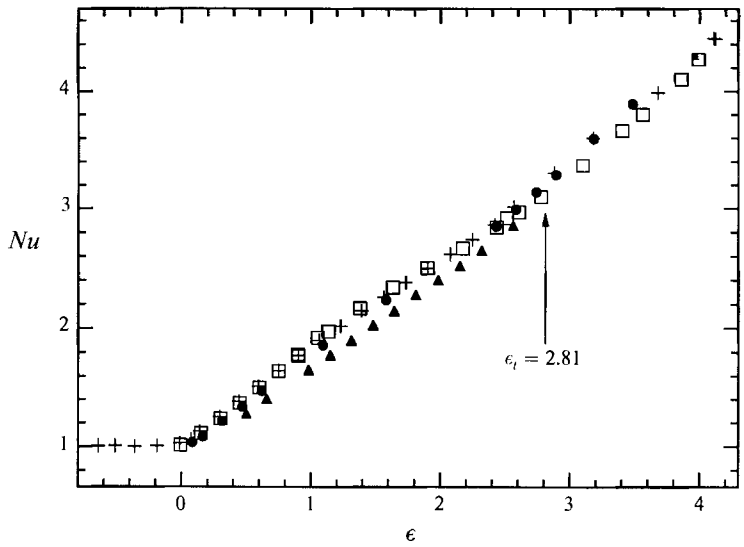


FIGURE 3. Nusselt numbers *vs.* $\epsilon$ at $\Omega = 2145$ for states starting at high $\epsilon$ with mode number 4 (□), 5 (+), 6 (●), and 7 (▲). The transition to noisy time dependence for mode 5 is indicated by a vertical arrow at $\epsilon_t = 2.81$.

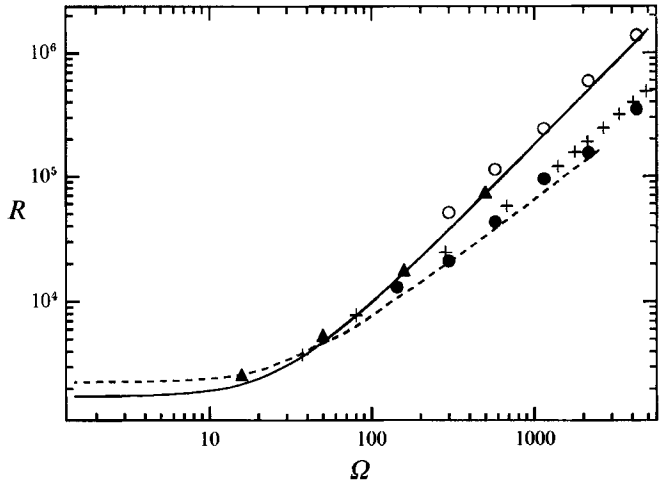


FIGURE 4. Stability diagram in $R$ *vs.* $\Omega$ parameter space. Solid line shows the prediction of linear stability calculations for the laterally infinite system and dashed line is linear analysis for asymmetric states in an $\Gamma = 1$ cylindrical container with insulating sidewall boundary conditions and for $\sigma = 6.7$ (after Goldstein *et al.* 1993). Data show the convective onset (●) and the onset of noisy time dependence (○). For comparison the onset data (+) of Rossby (1969) and calculations (▲) for axisymmetric states (Homsy & Hudson 1972) are shown.

experimental marginal stability curve. Rotation is predicted to suppress the onset of convection, pushing $R_c$ above its non-rotating value. In figure 4, the marginal stability curve for a laterally infinite system is shown in the parameter space of $R$ and $\Omega$ (Chandrasekhar 1961). Our results for the onset fall uniformly below those predictions but in good agreement with the data of Rossby (1969) for convection in water. This shift arises from the finite size geometry of the convection cell and agrees qualitatively (but not quantitatively, see below) with linear calculations of Buell & Catton (1983). Buell & Catton showed that modes localized near the outer boundary

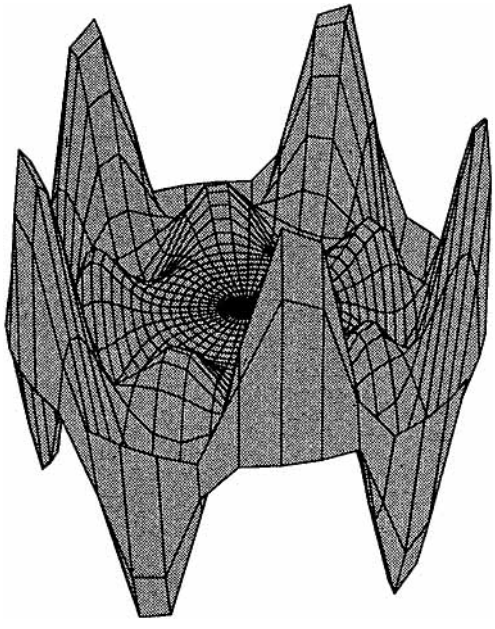

FIGURE 5. Numerical calculation of vertical velocity profile at the vertical mid-plane for an $m = 5$ azimuthal linear state. Courtesy of Rick Goldstein.

and having azimuthal periodicity were more unstable at lower $R$ than was the axisymmetric mode associated with the solution for the laterally infinite system calculated by Homsy & Hudson (1972). The onset values vary dramatically with sidewall boundary conditions since a conducting boundary tends to oppose the development of temperature gradients along the wall. The structure of these azimuthal states is shown in figure 5 for the midplane vertical velocity field of a 5-fold periodic state from a linear calculation using free–free top/bottom boundary conditions and rigid insulating sidewall boundary conditions by Goldstein *et al.* (1993). Experimental verification of these sidewall structures is shown in figure 6 for states with 4-, 5-, 6-, and 7-fold periodicity at $\Omega = 2145$. The data are digitally enhanced optical shadowgraph images where the darker shading indicates hotter, less dense fluid and the lighter shading is for the colder, more dense fluid. Slow ramping from the conduction state to the convection state yields $m = 5$. We therefore conclude that the critical mode for $\Omega = 2145$ is $m_c = 5$. The other states are produced by different history-dependent procedures including fast ramping or sudden jumps to high $\epsilon$-values. The states of $m = 4$, 5, 6 are stable in some band above onset whereas the $m = 7$ state is only metastable, existing for up to several vertical thermal diffusion times ($\tau_\kappa \equiv d^2/\kappa = 1.7 \times 10^4$ s). These data are consistent with the standard description of a stable band of wavenumbers in parallel roll convection. Also consistent with this picture is that the heat transport does not vary much with mode number. A detailed study of this issue in an aspect-ratio-2.5 convection cell shows excellent agreement with a complex Ginzburg–Landau amplitude equation description (Li & Ecke 1993). In the next section, we discuss the stability of the different modes relative to the conduction state and to the secondary states at higher $R$.

An interesting property of these azimuthally periodic states is that they propagate in the rotating frame, always in a direction opposite to the rotation direction. Such

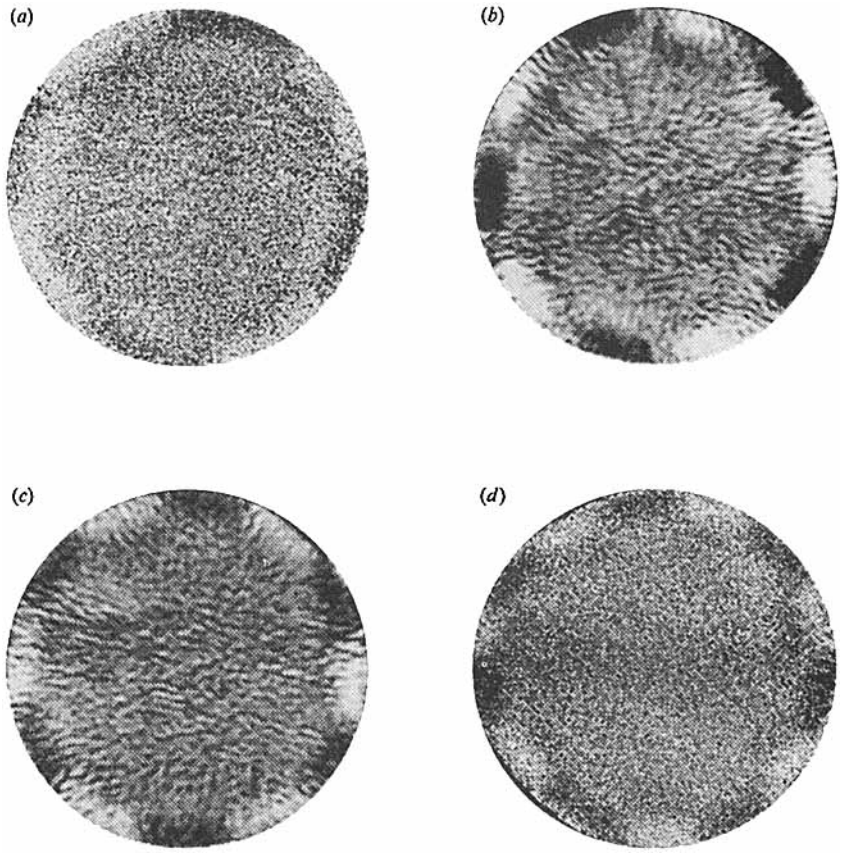


FIGURE 6. Shadowgraph images for $\Omega = 2145$ showing localized wall states with azimuthal $m$-fold periodicity: (*a*) $m = 4$, $\epsilon = 1.05$; (*b*) $m = 5$, $\epsilon = 0.84$; (*c*) $m = 6$, $\epsilon = 0.80$; (*d*) $m = 7$, $\epsilon = 0.66$.

behaviour was not expected and in fact the linear stability calculations of Buell & Catton (1983) assumed a stationary bifurcation. Relaxing that constraint, Goldstein *et al.* (1993) have recently shown that the solutions have a complex part and that the calculated precession frequencies are in good agreement with the experimental values. Their calculated critical onset values $R_c(\Omega)$ are also quite close to the experimental data, figure 4, whereas the results of Buell & Catton (1983) do not agree quantitatively with our data. In figure 7, the precession is illustrated in a space–time plot of the azimuthal intensity determined from images such as in figure 6. The shadowgraph intensity was taken near the outer sidewall at $0.9r_0$ over a radial band with $\delta r = 0.08r_0$. For $\epsilon < 2.80$ the precession was constant, figure 7(*a*), whereas for higher $\epsilon$ modulation of the precession speed was observed, figure 7(*b*).

The slope of the curve in these plots measures the phase velocity $v_p$ of an azimuthal travelling wave of the form $T(r, \phi, t) = f(r)\exp[\mathrm{i}(m\phi - \omega_p^m t)]$ where $\omega_p^m$ is the precession frequency of the $m$th mode and the phase velocity is given by $\omega_p^m/m$. In figure 8, we plot $\omega_p$ (dropping the explicit dependence on $m$) obtained from $v_p^m m$; the frequency appears to asymptote to a finite value at onset although the data only extend down to about $\epsilon = 0.3$. To expand this range we used two thermistors imbedded in the sidewall at the midplane, see figure 9, and oriented at about $2\pi/13$ radians from each other. As the wave propagated past the probes, the frequency was determined from a time series of either sensor and the mode number was obtained

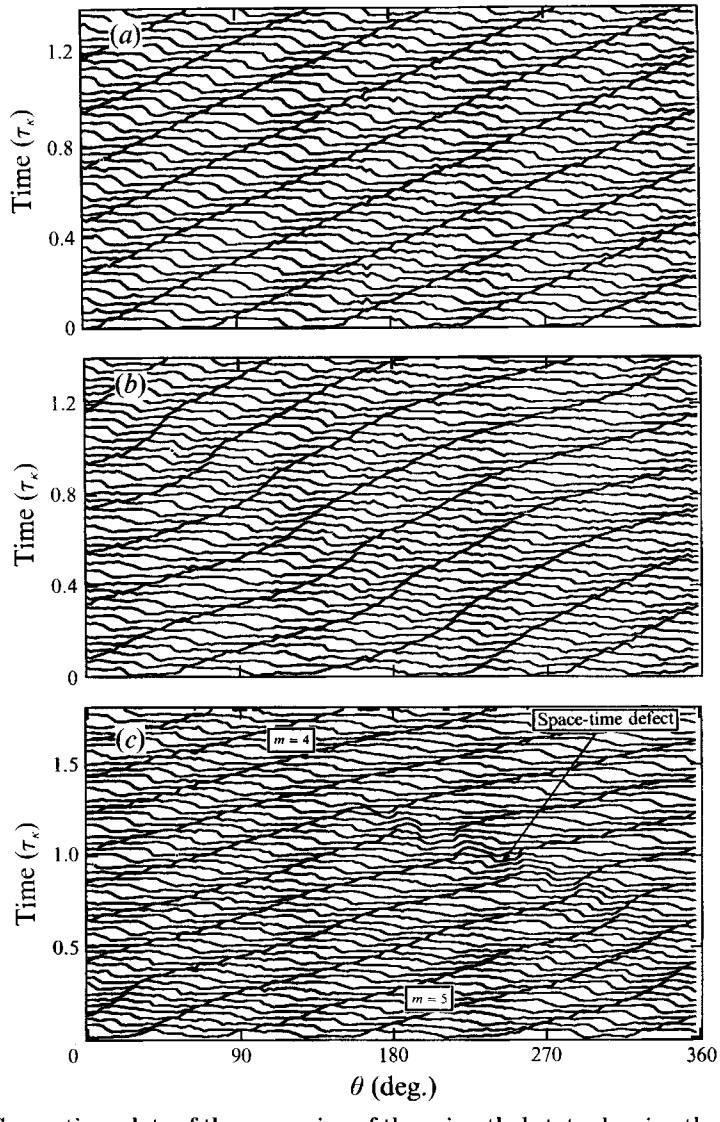


FIGURE 7. Space–time plots of the precession of the azimuthal state showing the radially averaged ($\delta r/r_0 = 0.08$) angular shadowgraph intensity at $r = 0.9r_0$ and for several values of $\epsilon$: (*a*) uniform precession, $m = 5$, $\epsilon = 2.80$, (*b*) modulated precession, $m = 5$, $\epsilon = 3.24$, (*c*) transition from $m = 5$ to $m = 4$ via a space–time dislocation, $\epsilon = 3.69$.

from the phase difference between the two signals. Using these probes we measured the amplitude, frequency, and mode number of the travelling wave down to $\epsilon = 0.01$. The amplitude varies like the square root of $\epsilon$, consistent with a Hopf bifurcation, figure 10(*a*), and the Nusselt number is linear in $\epsilon$, figure 10(*b*). The frequency varies linearly with $\epsilon$ with a finite intercept $\omega_0$ at onset, figure 10(*c*). This is different from the commonly observed Hopf bifurcation with O2 symmetry in which travelling waves in both directions are allowed. One can describe it, however, as a Hopf bifurcation arising when rotation breaks the reflection symmetry of the azimuthal mode (Ecke *et al.* 1992). This theory predicts that $\omega_0$ should vary linearly with $\Omega$ for small $\Omega$ and our measurements are consistent with that prediction and in quantitative agreement with the linear calculations of Goldstein *et al.* (1993), see

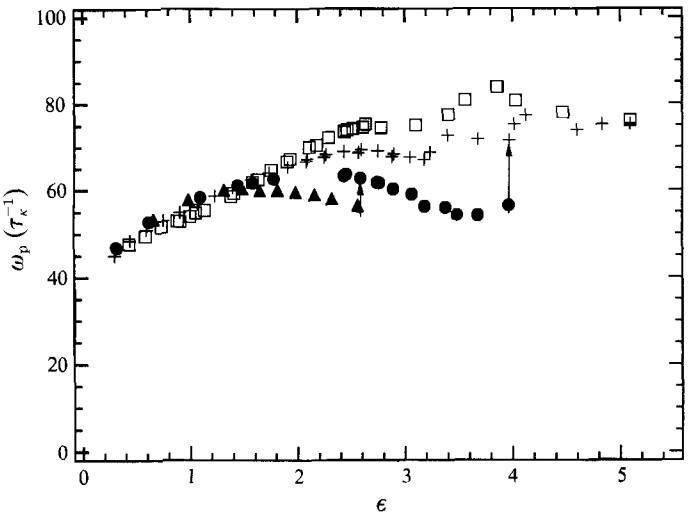


FIGURE 8. Azimuthal precession frequency $\omega_p$ *vs.* $\epsilon$ for $\Omega = 2145$ for different modes: $m = 4$ (□), $m = 5$ (+), $m = 6$ (●), and $m = 7$ (▲). Arrows indicate transitions between different modes.

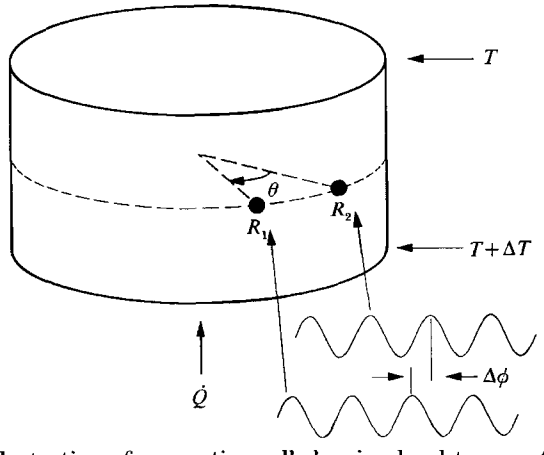


FIGURE 9. Schematic illustration of convection cell showing local temperature sensors located at the midplane. The physical angular separation of the probes is $2\pi/13$ radians.

figure 10(*d*). Recent measurements (Li & Ecke 1993) have verified this conjecture for $\Omega \geqslant 20$ in an aspect-ratio-2.5 convection cell. The data for $R_c$, $\omega_0$, and $m_c$ at $\Gamma = 1$ are tabulated in table 1.

The precession frequency depends only weakly on the mode number $m$ when $\epsilon \leqslant 1.5$ for $\Omega = 2145$. For higher $\epsilon$, however, large variations of $\omega_p$ with $m$ are seen, figure 8. In addition, transitions occur between states with different $m$. An example of a transition from an $m = 5$ state to an $m = 4$ state is shown in figure 7(*c*) where it appears as a space–time dislocation. These transitions define secondary stability boundaries in the parameter space of azimuthal wavenumber and $\epsilon$. These secondary instabilities are coincident with the convection pattern filling the entire cell, as opposed to being localized near the boundary, and with a change in slope of the Nusselt number curve. In the next section we describe the evolution of the centre-filling processes, the formation of thermal vortices, and the development of turbulent flow.

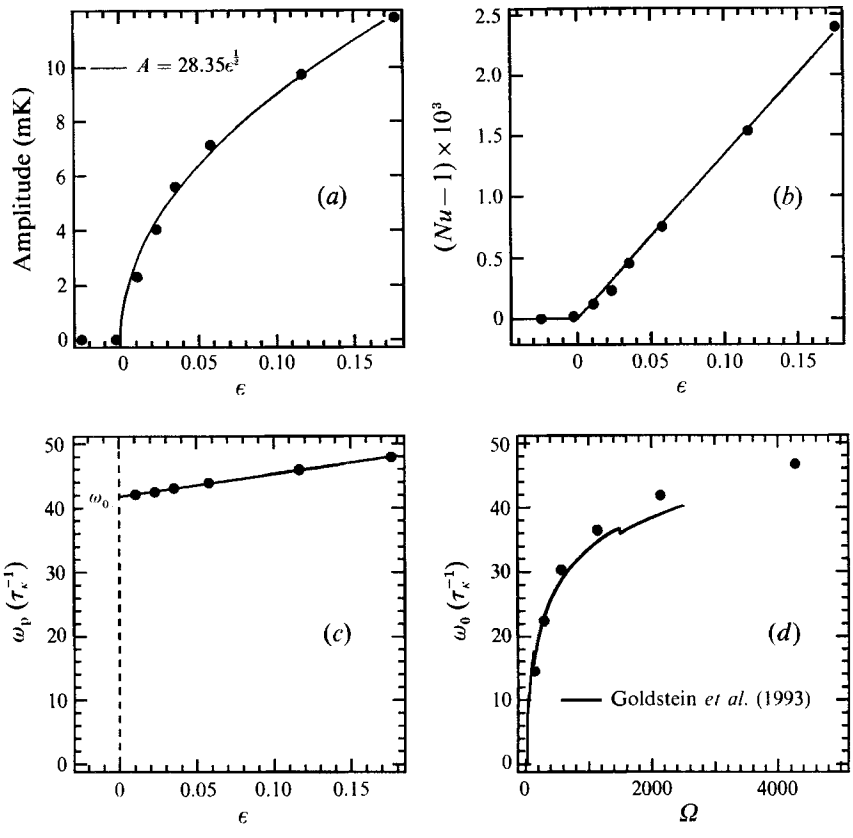


FIGURE 10. Plot of (*a*) the amplitude, (*b*) Nusselt number, and (*c*) frequency $\omega_p$ *vs.* $\epsilon$ close to onset. Solid curves are linear least-squares fits to the data. The linear dependence of the frequency and Nusselt number and the square-root dependence of the amplitude indicate a Hopf bifurcation. The $\epsilon = 0$ intercept of $\omega_p$ is denoted $\omega_0$ and is shown *vs.* $\Omega$ in (*d*). The behaviour of $\omega_0$ is consistent with a linear relationship for $\Omega < 100$. The linear calculation of Goldstein *et al.* (1993) for the calculated critical mode number is shown (solid curve) for comparison.

| $\Omega$ | $R_c$ $(10^4)$ | $\omega_0$ | $m_c$ |
|---|---|---|---|
| 143 | 1.294 | 14.45 | 3 |
| 296 | 2.097 | 22.4 | 4 |
| 572 | 4.273 | 30.3 | 4 |
| 1147 | 9.491 | 36.4 | 4, 5 |
| 2145 | 15.48 | 41.8 | 5 |
| 4274 | 34.68 | 46.7 | 5 |

TABLE 1. Values of $\Omega$, $R_c$, $\omega_0$, and $m_c$

## 4. Vortex states, heat transport, and turbulence

### 4.1. *Secondary instabilities*

For Rayleigh numbers several times the onset value the convective flow becomes more complex, both in space and in time. The quasi-one-dimensional azimuthal wave that is localized near the boundary for small $\epsilon$ spreads into the cell as spiral arms. At

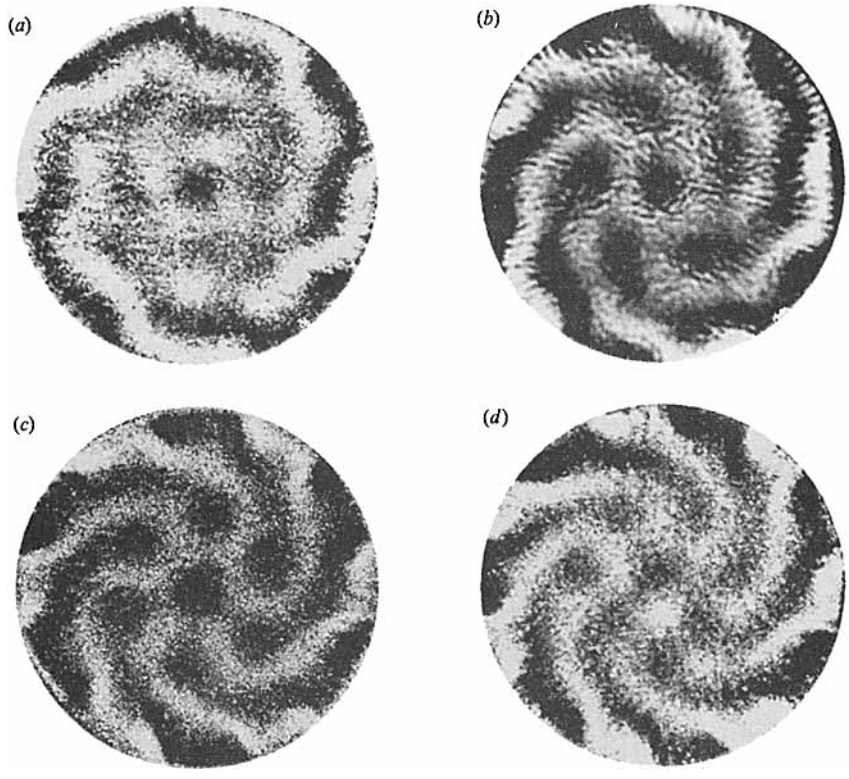


FIGURE 11. Shadowgraph images for $\Omega = 2145$ showing $m$-fold symmetric patterns: (*a*) $m = 4$, $\epsilon = 2.61$; (*b*) $m = 5$, $\epsilon = 2.59$; (*c*) $m = 6$, $\epsilon = 2.74$; (*d*) $m = 7$, $\epsilon = 2.56$.

the end of each arm a vortex forms as the cell fills completely so that a regular array of these vortices is present with the $m$-fold symmetry of the wall state, see figure 11. At about the same $\epsilon$-value, other signs that convection has been established throughout the cell are observed. In the heat transport measurements there is a distinct break in slope for $\epsilon \approx 2.8$, figure 3. Close to this parameter value the heat transport develops noisy time dependence as shown in figure 12 for different modes at $\Omega = 2145$. These secondary instability values $R_{c_0}$ are plotted in figure 4 and fall close to the linear stability curve for a laterally infinite system. It was not clear from these data whether this was a coincidence or indicative of ghosts of the axisymmetric or cell-filling states that are linearly unstable close to these parameter values. Recent investigation of this point in a cell with $\Gamma = 2.5$ show that this secondary instability is an indication of the linear instability of the inner regions of the cell where the sidewall-state amplitude is small and that the noisy time dependence arises from the KL instability (Li & Ecke 1993). We thus believe that the noisy time dependence in this more restricted geometry is a result of a finite-size KL transition. Also, the rotation is causing a vortex-like circulation of the flow for the centre-filling states so that we sometimes refer to this state as the vortex state.

The transitions between different mode-number states, the modulation of the precession frequency of the sidewall states, the appearance of aperiodic time-dependent heat transport, and the distinct change in slope in the Nusselt number curves indicate regions of stability for the states with different $m$. In figure 13, these primary and secondary instability boundaries are indicated for $\Omega = 2145$ in the

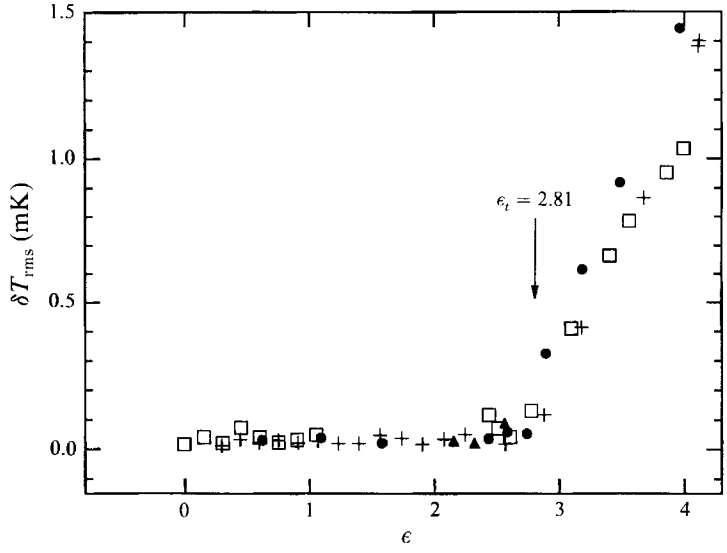


FIGURE 12. RMS temperature fluctuations $\delta T_{\rm rms}$ in the bottom plate *vs.* $\epsilon$ showing the transition to noisy time dependence. Data for different mode numbers are shown: $m = 4$ (□), $m = 5$ (+), $m = 6$ (●), and $m = 7$ (▲).

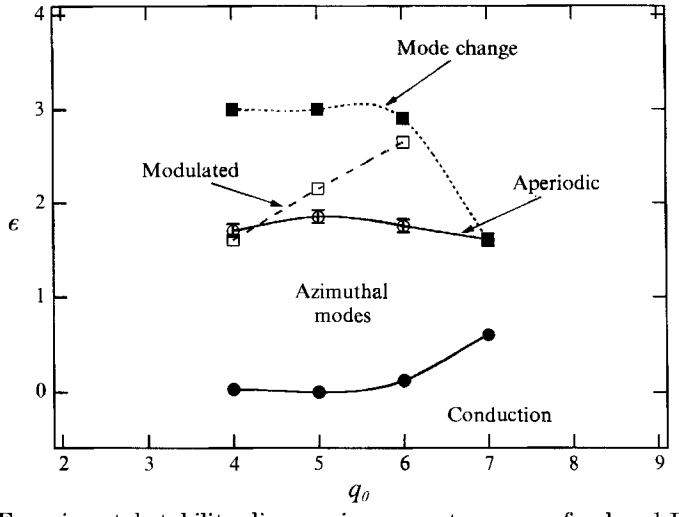


FIGURE 13. Experimental stability diagram in parameter space of reduced Rayleigh number and azimuthal wavenumber $q_\theta$ for $\Omega = 2145$. Solid and dashed lines are guides to the eye.

parameter space of $\epsilon$ and dimensionless azimuthal wavenumber, defined as $q_\theta \equiv m(d/r_0) = m/\Gamma$, where $m$ is the periodicity of the azimuthal mode. The bottom boundary separates convection and conduction regions and was obtained by decreasing $\epsilon$ from above onset while in a particular $m$-fold symmetric state. Thus the boundary is the nonlinear stability boundary for the convection state. The other boundaries are the transition to aperiodic time dependence, for which there is not much $\epsilon$ variation with $m$, the observed transitions between states with different $m$ such as illustrated in figures 7(*c*) and 8, and the modulation of the precession

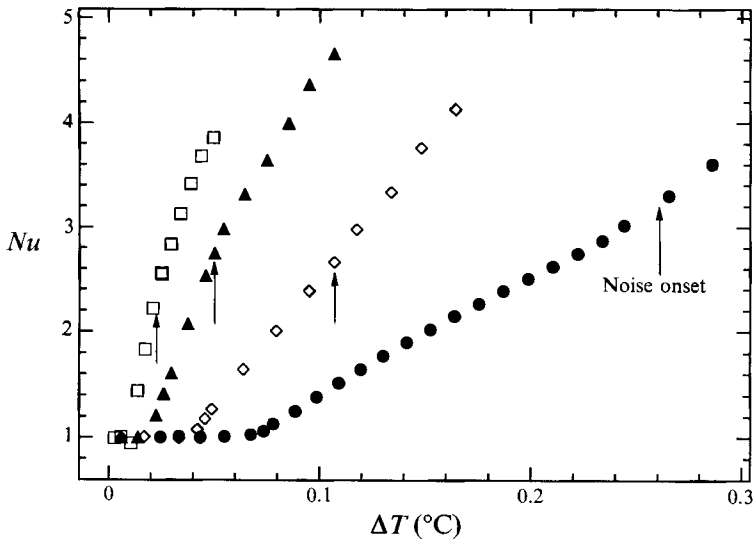


FIGURE 14. *Nu vs.* $\Delta T$ for $\Omega = 296$ (□), $\Omega = 572$ (▲), $\Omega = 1147$ (◇), $\Omega = 2145$ (●).

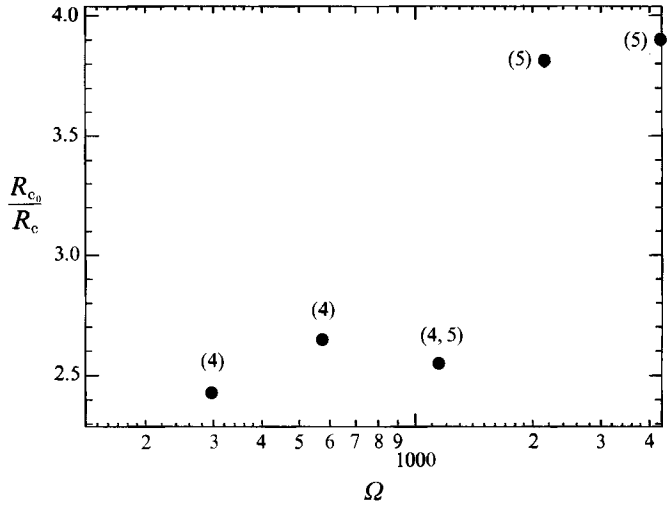


FIGURE 15. Ratio of Rayleigh number for onset of time dependence $R_{c_0}$ to onset Rayleigh number $R_c$ for various values of $\Omega$. Numbers in brackets show the critical values of $m$ at onset.

frequency of the sidewall states, figure 7(*b*). The slope-change boundary is not distinguishable from that determined by the appearance of aperiodic heat transport on the scale presented here.

A partial characterization of these states for different $\Omega$-values is provided by heat transport data. In figure 14, we show $Nu$ versus $\Delta T$ for different $\Omega$ in the range of control parameter close to the transition to the vortex states. From these data and the noisy-onset data we determine the onset values for convection, $R_c$ and for the vortex state, $R_{c_0}$. The ratio of these two values is plotted in figure 15 and shows a distinct change for $\Omega \approx 1000$. This change most likely corresponds to the increase in the critical value of $m$ at onset from 4 to 5, which strongly affects the primary bifurcation but only weakly shifts the secondary transition.

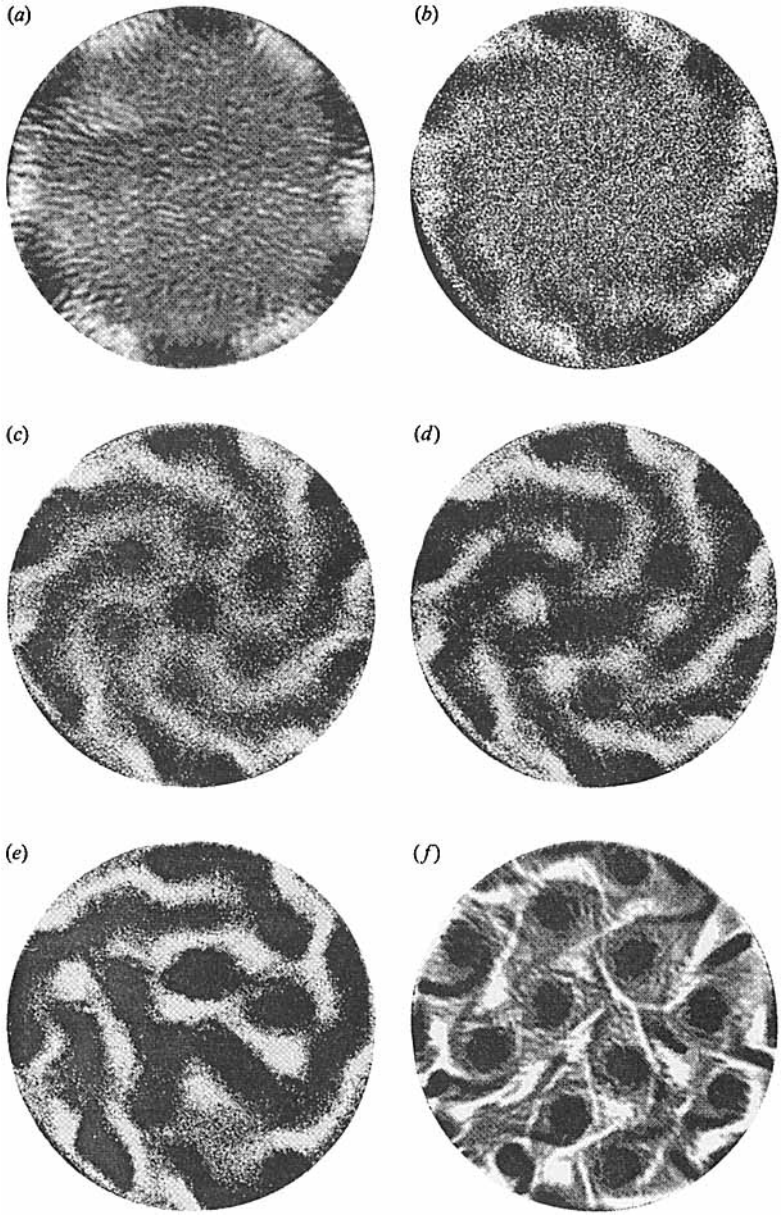


FIGURE 16. Shadowgraph images for $\Omega = 2145$ showing evolution of the convective state with increasing $\epsilon$. Mode 6 is the azimuthal mode number for states with $\epsilon < 3.2$ (note that while the critical mode number is 5, mode 6 exists over a large range $0.1 < \epsilon < 3.7$). For $\epsilon = 3.97$ there has been a transition to a mode-5 state. (*a*) $\epsilon = 0.8$, $Nu = 1.59$; (*b*) $\epsilon = 1.58$, $Nu = 2.23$; (*c*) $\epsilon = 2.74$, $Nu = 3.14$; (*d*) $\epsilon = 3.19$, $Nu = 3.59$; (*e*) $\epsilon = 3.97$, $Nu = 4.30$; (*f*) $\epsilon = 15.80$, $Nu = 11.76$.

### 4.2. *Vortex interactions*

Further increases of $R$ produce increasingly complex states where the patterns are constantly changing. In figure 16, a series of shadowgraph images for $\Omega = 2145$ at successively larger $\epsilon$ in the range $0.80 < \epsilon < 12$, shows a progressive evolution of behaviour. At the highest $\epsilon = 15.80$ ($R = 2.6 \times 10^6$) the flow is turbulent and the remaining thermal vortices undergo significant interactions resulting in complex

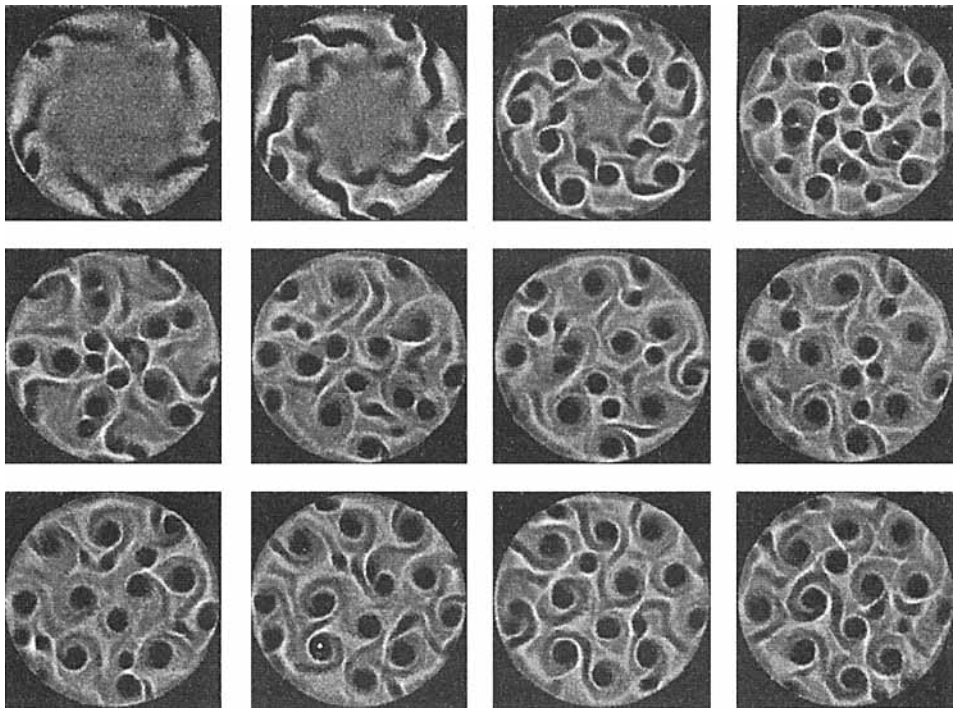

FIGURE 17. Time evolution of vortices from weakly convecting state with azimuthal sidewall state with $m = 5$ for $\Omega = 2145$ and $R \approx 7 \times 10^6$. The time separation between images is about $15\tau_R$ ($\tau_R = 6.4$ s) and the sequence of images proceeds from upper left to lower right.

dynamics. A particularly interesting way to study the evolution and interactions of vortices is to investigate transients that arise from suddenly applying additional heat to a conducting or weakly convecting state. Such a transient sequence is shown in figure 17. The timescale for these dynamics is rapid on the thermal diffusion timescale $\tau_\kappa = 1.7 \times 10^4$ s and thus we present them in terms of a turbulent time $\tau_R \equiv \tau_\kappa / R^{\frac{1}{2}}$. During the initial stages, vortices formed rapidly but were constrained by the symmetry of the sidewall state; there is 5-fold symmetry to the vortex pattern for figures 17(*a*)–17(*d*). After the maximum density of vortices was reached, see figure 17(*d*), the number decreased until a steady state was attained. The steady state is a dynamical balance between nucleation events occurring at or near the sidewalls and annihilations (mergings) of vortices that take place in the interior region of the convection cell. An example of this vortex merging is shown in figure 18 and a quantitative characterization of the merging is shown in figure 19(*a*, *b*), where the separation $\delta r/a_0$ ($a_0$ is the size of a single vortex and is about $d/5$) and the relative angular orientation of the two vortices are plotted versus time. There appears to be two distinct regimes of behaviour, the first being a uniform rotation of the two vortices without noticeable decrease in separation. The circulation then increases suddenly and the two vortices quickly approach each other to form a single vortex. Another example from the same transient sequence, is shown in figure 19(*c*, *d*). Finally, in figure 20, the interactions and merging of three vortices is illustrated. Two of the vortices merge first and then spiral around the third which remains relatively immobile during this process. There has been significant work on two-dimensional vortex merger (see for example Melander, Zabusky & McWilliams, 1988) but none that we are aware of on thermal vortices.

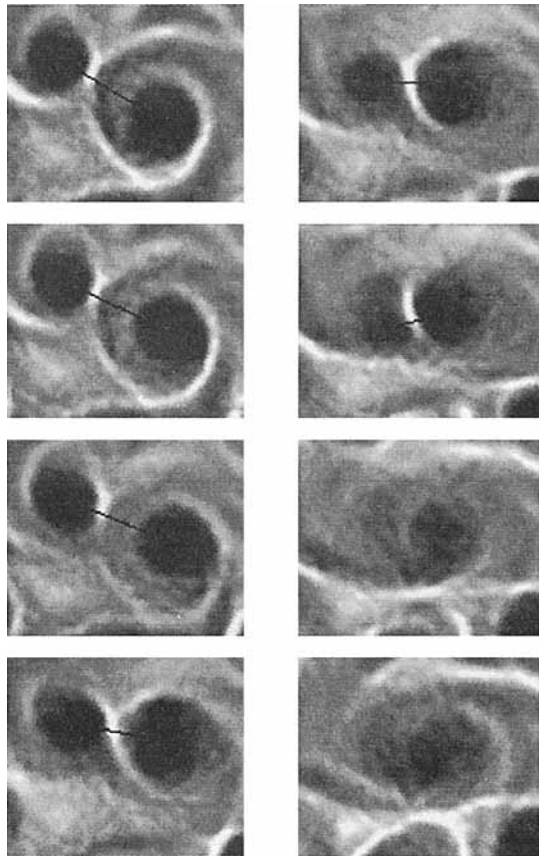

FIGURE 18. Time evolution of vortices showing vortex merging for $\Omega = 2145$ and $R = 7 \times 10^6$. The time separation between images is about $3\tau_R$ ($\tau_R = 6.4$ s) and the time sequence proceeds from upper left to lower right.

### 4.3. *Turbulent heat transport*

Finally, we discuss the scaling of the heat transport with Rayleigh number in the turbulent regime. Recent experimental progress on turbulent convection has distinguished a transition between 'soft' and 'hard' turbulence that shows up in the probability distribution function (PDF) of temperature fluctuations in the middle of the convection cell (Heslot *et al.* 1987). For small-aspect-ratio convection cells ($\Gamma \leqslant 1$), this transition from Gaussian to exponential PDFs is accompanied by a change in the exponent of the power-law scaling of the heat transport, $Nu = AR^{\beta}$. For convection in helium with Prandtl number about 0.7 the exponent $\beta$ takes the classical value (Malkus 1954*a*, *b*; Howard 1966) of $\frac{1}{3}$ in the soft regime for $R < 2 \times 10^6$ whereas for hard turbulence with $R > 2 \times 10^7$, $\beta = \frac{2}{7} = 0.286$. Two theories have been suggested to explain the $\frac{2}{7}$ exponent of the heat transport scaling at high Rayleigh number. Castaing *et al.* (1989) introduced the concept of a mixing zone that is much larger than the thermal boundary layer but still significantly smaller than the cell height. In this model heat from the boundary layer is effectively transferred through the mixing zone by temperature and velocity fluctuations in the form of eruptions of thermal plumes from the boundary layer. The difference between the soft and hard turbulence regimes arises from the different spatial and temporal behaviour of these coherent structures. In the soft regime they extend over large distances and appear

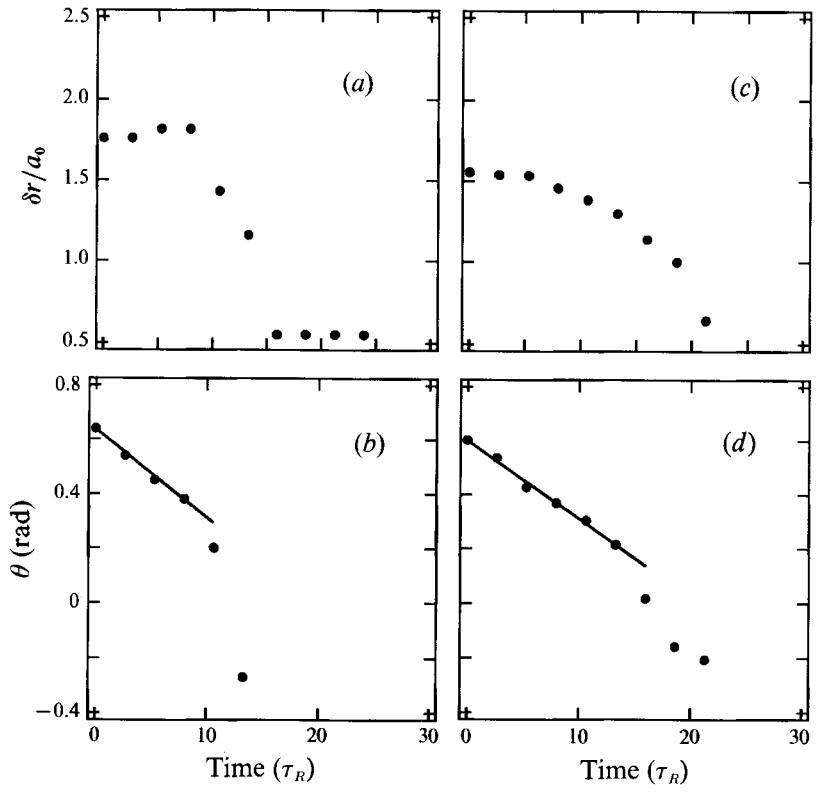


FIGURE 19. (*a*) Separation $\delta r/a_0$ and (*b*) angular orientation $\theta$ *vs.* time for two merging vortices, where $a_0$ is the characteristic size of a single vortex. Data are the same as for figure 18. Another example of merging vortices is shown in (*c*, *d*): (*c*) $\delta r/a_0$ and (*d*) *vs.* time. Straight line fits of $\theta$ in (*b*) and (*d*) indicate uniform rotation.

as rare but strong eruptions whereas in the hard regime they break into pieces, appearing more frequently and with more regularity in both space and time. These different characteristics then imply the Gaussian or exponential PDFs of the soft or hard turbulence regimes. The second theory, of Shraiman & Siggia (1990), is based on the physical assumption that the heat transport is controlled by a thermal boundary layer that is created by the shear flow near the walls. This assumption is valid when the entire temperature drop occurs within the viscous sublayer of the turbulent boundary layer and is therefore dependent on the ratio of viscous to thermal lengthscales. The implication of this is that the $\beta = \frac{2}{7}$ scaling regime will vary with the Prandtl number in such a manner as to extend the bottom limit of hard-turbulence scaling to higher $R$ for higher $\sigma$.

Several of the concepts that distinguish the two theoretical models have recently been tested by Solomon & Gollub (1990). They showed that although the form of the thermal plumes was strongly modified by externally induced horizontal shear in the boundary layer, no significant increase in $Nu$ was observed. In addition, they investigated the role of induced recirculating flows (Solomon & Gollub 1991) and found that additional mixing produced by these flows led to a large enhancement of $Nu$ (up to 70%). These experiments favour the model of Shraiman & Siggia which makes no specific assumptions about the structure of thermal plumes or about the stability of the boundary layer.

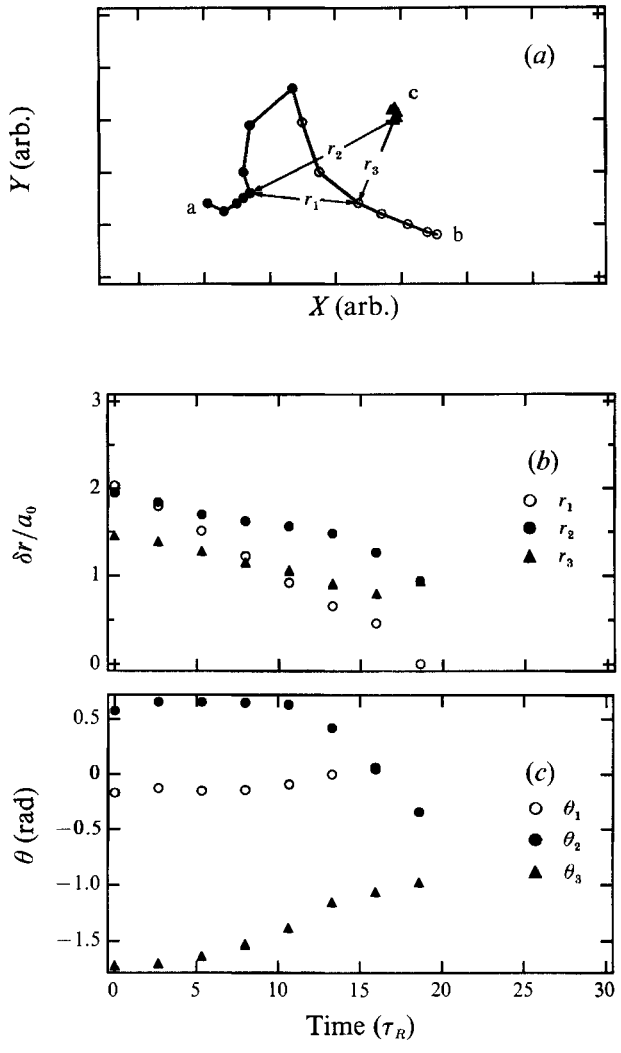


FIGURE 20. (*a*) Trajectories of three vortices labelled a, b, c with separations $r_1$, $r_2$, and $r_3$ as indicated in the figure; (*b*) separations $\delta r/a_0$ of the three vortices; (*b*) angular orientation $\theta$ of three vortices undergoing merger. Data are from the same sequence as in figure 18.

The influence of rotation on the general problem of turbulent convection has not been considered in the same framework as discussed above. From that perspective rotation adds a number of interesting features that might prove useful in understanding the role of thermal plumes and recirculating flows in turbulent convection. The main advantage of rotation is that it provides an additional control parameter $\Omega$ that acts to generate a natural vortical motion in the fluid as opposed to the externally induced motions used by Solomon & Gollub (1990, 1991). Rotation can also contribute an additional body force through centrifugal acceleration which might modify the scaling behaviour of the heat transport. A recent theory of L'vov (1991) that considers turbulent scaling as being determined by the conserved quantities in the problem might be extended to include the effects of rotation. Simple considerations suggest that the Coriolis force will not change the exponent of the scaling because it does not contribute to the energy in the Navier–Stokes equation

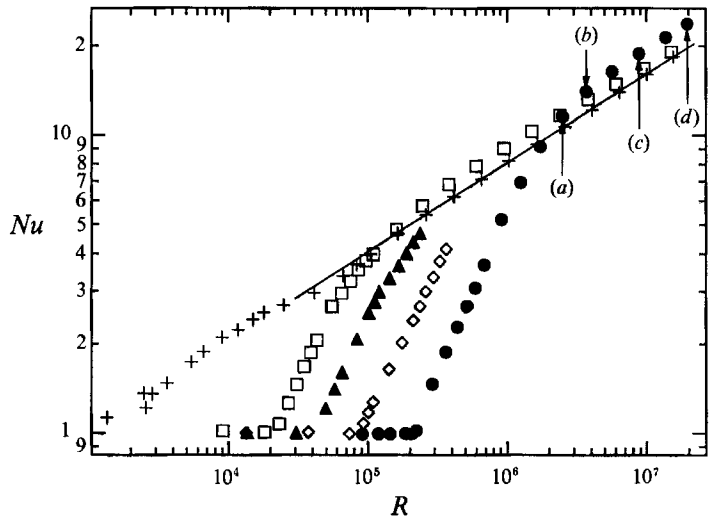


FIGURE 21. *Nu vs. R* for $\Omega = 0$ (+), $\Omega = 296$ (□), $\Omega = 572$ (▲), $\Omega = 1147$ (◇), $\Omega = 2145$ (●). Solid line is the linear, least-squares fit for $\Omega = 0$ data and yields a scaling exponent of $0.299 \pm 0.003$. Labels (*a–d*) refer to figure 22.

| $A$ | $\alpha$ | $R$-Range | $\Gamma$ | Reference |
|---|---|---|---|---|
| 0.131 | 0.300 (5) | $3 \times 10^4$–$2 \times 10^6$ | 1.4–5 (C) | Rossby (1969) |
| 0.183 | 0.278 | $3 \times 10^5$–$10^8$ | 1.5–6.0 (C) | Chu & Goldstein (1973) |
| 0.145 | 0.29 | $3 \times 10^7$–$4 \times 10^9$ | 3.5–14 (S) | Tanaka & Miyata (1980) |
| 0.129 | 0.299 (3) | $10^5$–$2 \times 10^7$ | 1.0 (C) | This work |
| 0.137 | 0.275 (7) | $2 \times 10^6$–$2 \times 10^8$ | 0.71, 1.6 (S) | Solomon & Gollub (1991) |

TABLE 2. Values of heat transport scaling parameters: $A$, $\alpha$, $R$-Range, $\Gamma$ (C = cylindrical, S = square with $\Gamma = L/d$), and reference

(it should substantially modify the prefactor). On the other hand the centrifugal terms will change the energy balance and therefore should influence the scaling exponent directly. In this experiment centrifugal effects were minimized and should play no role in the exponent but in future work sufficiently strong centrifugal accelerations should be applied to test the theory.

In this work we show data and shadowgraph images that are suggestive of a number of the features expected from the theoretical descriptions and that set the stage for more thorough studies that will include measurements of PDFs using local temperature probes. In particular, we first consider the influence of rotation on the dependence of $Nu$ on $R$ for large values of $R$, see figure 21. The non-rotating data scale like $Nu = AR^{\beta}$ with an exponent $\beta = 0.299 \pm 0.003$ (the errors reflect statistical errors in the least-squares fit and do not include possible systematic errors) and a prefactor $A = 0.129$. The scaling exponent $\beta$ has been measured in water by a number of investigators. Experiments by Rossby (1969), Chu & Goldstein (1973), Tanaka & Miyata (1980), and Solomon & Gollub (1991) yielded values in the range $0.129 < A < 0.18$ and $0.275 < \beta < 0.300$. Specific values are listed in table 2. In general the values for the scaling exponent fall below the classical $\frac{1}{3}$ value but slightly above the $\frac{2}{7}$ scaling found in helium experiments (Wu & Libchaber 1992). This may be due to the limited range of $R$ used to determine $\beta$ or because, for the higher Prandtl number

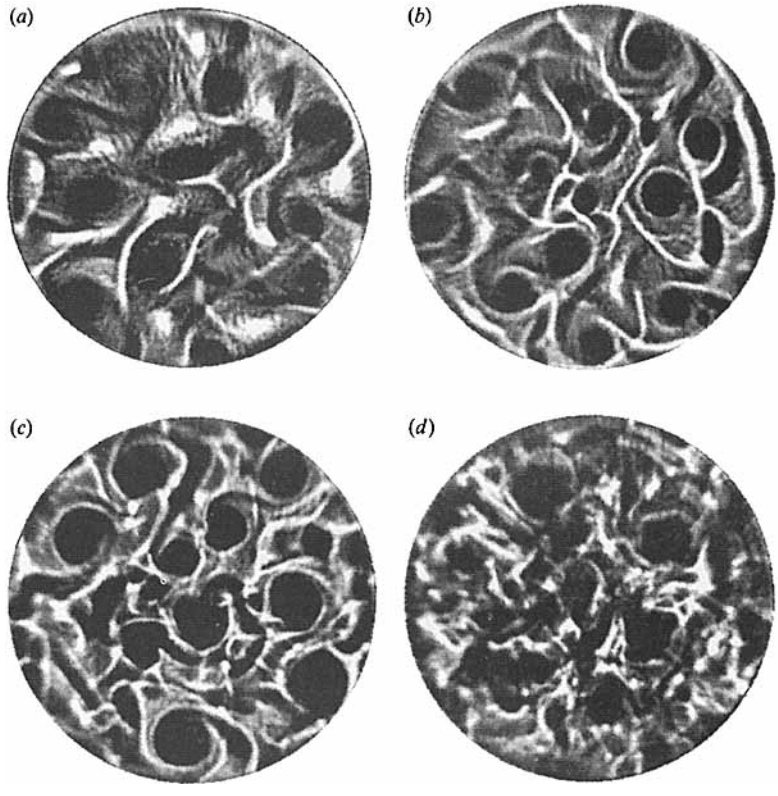


FIGURE 22. Images for $\Omega = 2145$ corresponding to heat transport data in figure 21 at various values of $R$: (*a*) $2.5 \times 10^6$; (*b*) $3.7 \times 10^6$; (*c*) $8.8 \times 10^6$; (*d*) $2.0 \times 10^7$.

of water, the scaling range may be pushed to higher $R$ as suggested by Shraiman & Siggia (1990). In future work we will extend the range of $R$ to better test the scaling law.

Next we consider the influence of rotation on the scaling of the Nusselt number. Rotation suppresses the onset of convection but $Nu$ rises rapidly and actually surpasses the non-rotating heat transport value, figure 21. Asymptotically, the heat transport for rotating flows appears to approach the non-rotating curve from above, either merging with the non-rotating data for large $R$ or providing a uniform shift to higher $Nu$. We expect that a uniform shift is most likely as the vortices provide additional recirculating flow and possible Eckmann suction, either of which could disrupt the boundary layer thereby enhancing the heat transport. In this context it is interesting to consider images of convection at different points along the Nusselt number curve for $\Omega = 2145$. Each image in figure 16 can be associated with $Nu$ data in figure 21. Further, a series of four shadowgraph images shown in figure 22 and labelled in figure 21 indicate how rotation imposes a coherence on the thermal structures even at quite high Rayleigh numbers. A final point about the Nusselt scaling with rotation is that the dimensionless rotation rate does vary substantially (10–15%) owing to our method of fixed $T_{top}$ and fixed dimensional rotation rate, $\Omega_D$. Such variations could have a quantitative influence on the results, although the qualitative features should remain. Therefore, no systematic effort to extract scalings for the rotating data has been made. Future measurements will correct this

effect by using constant-$\Delta T$ conditions and correcting $\Omega_D$ at each point so that $\Omega$ remains constant. A larger range in $R$ will also be studied so as to investigate the asymptotic behaviour of the heat transport scaling.

## 5. Conclusions

We have investigated the onset and evolution of states in a unity-aspect-ratio convection cell, acted upon by rotation-induced Coriolis forces. The onset modes are shown to be azimuthally periodic and localized near the lateral boundary. The results are in qualitative agreement with linear calculations of Buell & Catton (1983). In addition the $m$-fold periodic states are observed to precess in the rotating frame, consistent with a theory based on bifurcations with symmetry. Specifically, rotation breaks weakly the reflection symmetry of the azimuthally periodic states and induces a precession whose frequency increases from zero as $\Omega$ increases from zero. At finite $\Omega$ the dependence of amplitude and frequency for the travelling wave state vary as one would expect for a Hopf bifurcation. This state is thus a one-dimensional travelling wave and interesting instabilities occur as $R$ is increased. The predictions of linear theory (Goldstein *et al.* 1993) for the precession frequency and for the onset Rayleigh numbers agree quite well with experimental results. Their calculations also predict the size (aspect ratio) dependence of these onset modes. Recent results of Li & Ecke (1993) show that for $\Gamma = 2.5$, the quantities $\omega_p$, $R_c(\Omega)$, and the dimensionless azimuthal wavenumber are not changed much by the aspect ratio change, also in agreement with theory. The stability of the azimuthal modes relative to the axisymmetric modes and the laterally infinite states needs further experimental study to resolve the role of aspect ratio in the nonlinear states at onset and on the Nusselt number dependence of these states.

For higher $R$ we have made a good survey of the nonlinear states and their properties. The fluid begins to convect throughout the cell and irregular dynamics appear. As the convective amplitude increased, localized vortices were formed. Vortex interactions and mergers were observed that balanced the nucleation of vortices at the sidewalls. At still higher $R$ these vortices become less distinct as the flow becomes more turbulent. This progression to turbulence is strongly influenced by the rotation but the final states at very high $R$ do not seem much affected (at least as measured in the scaling of the heat transport). More experimental measurements are necessary to investigate the novel features of turbulence in rotating thermal convection.

We are grateful for support from the US Department of Energy and wish to acknowledge useful discussions with Guenter Ahlers, Mike Cross, Rick Goldstein, Yu-Chou Hu, Edgar Knobloch, Ning Li, Ronnie Mainieri, Thierry Passot, Mary Silber, and Laurette Tuckerman. We would like to express special thanks to Timothy Sullivan for experimental assistance and helpful advice.

## REFERENCES

Boubnov, B. M. & Golitsyn, G. S. 1986 Experimental study of convective structures in rotating fluids. *J. Fluid Mech.* **167**, 503–531.

Boubnov, B. M. & Golitsyn, G. S. 1990 Temperature and velocity field regimes of convective motions in a rotating plane fluid layer. *J. Fluid Mech.* **219**, 215 239.

Buell, J. C. & Catton, I. 1983 Effects of rotation on the stability of a bounded cylindrical layer of fluid heated from below. *Phys. Fluids* **26**, 892–896.

BUSSE, F. H. 1981 Transition to turbulence in Rayleigh–Bénard convection. In *Hydrodynamic Instabilities and the Transition to Turbulence* (ed. H. L. Swinney & J. P. Gollub), pp. 97–137. Springer.

CASTAING, B., GUNARATNE, G., HESLOT, F., KADANOFF, L., LIBCHABER, A., THOMAE, S., WU, X.-Z., ZALESKI, S. & ZANETTI, G. 1989 Scaling of hard thermal turbulence in Rayleigh–Bénard convection. *J. Fluid Mech.* **204**, 1–20.

CHANDRASEKHAR, S. 1953 The instability of a layer of fluid heated below and subject to Coriolis forces. *Proc. R. Soc. Lond.* A **217**, 306–327.

CHANDRASEKHAR, S. 1961 *Hydrodynamic and Hydromagnetic Stability.* Oxford University Press.

CHARLSON, G. S. & SANI, R. L. 1970 Thermoconvective instability in a bounded cylindrical fluid layer. *Intl J. Heat Mass Transfer* **13**, 1479–1496.

CHU, T. H. & GOLDSTEIN, R. J. 1973 Turbulent convection in a horizontal layer of water. *J. Fluid Mech.* **60**, 141–159.

CROQUETTE, V. 1986 Thesis, Université de Paris.

ECKE, R. E., ZHONG, F. & KNOBLOCH, E. 1992 Hopf bifurcation with broken reflection symmetry in rotating Rayleigh–Bénard convection. *Europhys. Lett.* **19**, 177–182.

FERNANDO, H. J. S., CHEN, R. & BOYER, D. L. 1991 Effects of rotation on convective turbulence. *J. Fluid Mech.* **228**, 513–547.

GOLDSTEIN, H. F., KNOBLOCH, E., MERCADER, A. & NET, M. 1993 Convection in a rotating cylinder. Part 1. Linear theory for moderate Prandtl numbers. *J. Fluid Mech.* **248**, 583–604.

HESLOT, F., CASTAING, B. & LIBCHABER, A. 1987 Transitions to turbulence in helium gas. *Phys. Rev.* A **36**, 5870–5873.

HOMSY, G. H. & HUDSON, J. L. 1972 Stability of a radially bounded rotating fluid heated from below. *Appl. Sci. Res.* **26**, 53–67.

HOWARD, L. N. 1966 Convection at high Rayleigh number. In *Applied Mechanics, Proc. 11th Intl Congr. of Applied Mechanics, Munich (Germany)* (ed. H. Gortler). Springer.

*International Critical Tables of Numerical Data, Physics, Chemistry, and Technology* 1930 US National Research Council, McGraw-Hill.

KOLODNER, P. & WILLIAMS, H. 1990 Complex demodulation techniques for experiments on traveling wave convection. In *Nonlinear Evolution of Spatio-Temporal Structures in Dissipative Continuous Systems*, Vol. 225 NATO ASI Series B2 (ed. F. Busse & L. Kramer), pp. 73–91. Plenum.

KÜPPERS, G. 1970 The stability of steady finite amplitude convection in a rotating fluid. *Phys. Lett.* A **32**, 7–8.

KÜPPERS, G. & LORTZ, D. 1969 Transition from laminar convection to thermal turbulence in a rotating fluid layer. *J. Fluid Mech.* **35**, 609–620.

LI, N. & ECKE, R. 1993 Rotating Rayleigh–Bénard convection: aspect ratio dependence of the initial bifurcations. *Phys. Rev.* E (to appear).

L'VOV, V. S. 1991 Spectra of velocity and temperature fluctuations with constant entropy flux of fully developed free-convective turbulence. *Phys. Rev. Lett.* **67**, 687–690.

MALKUS, W. V. R. 1954*a* Discrete transitions in turbulent convection. *Proc. R. Soc. Lond.* A **225**, 185–195.

MALKUS, W. V. R. 1954*b* The heat transport and spectrum of thermal turbulence. *Proc. R. Soc. Lond.* A **225**, 196–212.

MELANDER, M., ZABUSKY, N. & MCWILLIAMS, F. 1988 Symmetric vortex merger in two dimensions: causes and conditions. *J. Fluid Mech.* **195**, 303–340.

MEYER, C. W. 1988 Patterns in time-dependent Rayleigh–Bénard convection experiments. PhD thesis, UC Santa Barbara.

NAKAGAWA, Y. & FRENZEN, P. 1955 A theoretical and experimental study of cellular convection in rotating fluids. *Tellus* **7**, 1–21.

PFOTENHAUER, J. M., NIEMELA, J. J. & DONNELLY, R. J. 1987 Stability and heat transfer of rotating cryogens. Part 3. Effects of finite cylindrical geometry and rotation on the onset of convection. *J. Fluid Mech.* **175**, 85–96.

RAASCH, S. & ETLING, D. 1992 Numerical simulation of rotating turbulent thermal convection. *Contr. Atmos. Phys.* **3**, 191–205.

ROSSBY, H. T. 1969 A study of Bénard convection with and without rotation. *J. Fluid Mech.* **36**, 309–337.

SHRAIMAN, B. I. & SIGGIA, E. D. 1990 Heat transport in high-Rayleigh-number convection. *Phys. Rev.* A **42**, 3650–3653.

SOLOMON, T. H. & GOLLUB, J. P. 1990 Sheared boundary layers in turbulent Rayleigh–Bénard convection. *Phys. Rev. Lett.* **64**, 2382–2385.

SOLOMON, T. H. & GOLLUB, J. P. 1991 Thermal boundary layers and heat flux in turbulent convection: The role of recirculating flows. *Phys. Rev.* A **43**, 6683–6693.

STORK, K. & MÜLLER, U. 1975 Convection in boxes: an experimental investigation in vertical cylinders and annuli. *J. Fluid Mech.* **71**, 231–240.

TANAKA, H. & MIYATA, H. 1980 Turbulent natural convection in a horizontal water layer heated from below. *Intl J. Heat Mass Transfer* **23**, 1273–1281.

THRELFALL, D. C. 1975 Free convection in low temperature gaseous helium. *J. Fluid Mech.* **67**, 17–28.

VERONIS, G. 1959 Cellular convection with finite amplitude in a rotating fluid. *J. Fluid Mech.* **5**, 401–435.

WU, X.-Z. & LIBCHABER, A. 1992 Scaling relations in thermal turbulence: The aspect-ratio dependence. *Phys. Rev.* A **45**, 842–845.

ZHONG, F., ECKE, R. & STEINBERG, V. 1991 Rotating Rayleigh–Bénard convection: Asymmetric states and the transition to vortex structures. *Phys. Rev. Lett.* **67**, 2473–2476.